
Generating camera failures as a class of physics-based adversarial examples

Manav Prabhakar* Jwalandhar Girnar* Arpan Kusari†
University of Michigan Transportation Research Institute
University of Michigan
Ann Arbor, MI - 48103
{prmanav, jwala, kusari}@umich.edu

Abstract

While there has been extensive work on generating physics-based adversarial samples recently, an overlooked class of such samples come from physical failures in the camera. Camera failures can occur as a result of an external physical process, i.e. breakdown of a component due to stress, or an internal component failure. In this work, we develop a simulated physical process for generating broken lens as a class of physics-based adversarial samples. We create a stress-based physical simulation by generating particles constrained in a mesh and apply stress at a random point and at a random angle. We perform stress propagation through the mesh and the end result of the mesh is a corresponding image which simulates the broken lens pattern. We also develop a neural emulator which learns the non-linear mapping between the mesh as a graph and the stress propagation using constrained propagation setup. We can then statistically compare the difference between the generated adversarial samples with real, simulated and emulated adversarial examples using the detection failure rate of the different classes and in between the samples using the Frechet Inception distance. Our goal through this work is to provide a robust physics based process for generating adversarial samples.

1 Introduction

Cameras are ubiquitous as remote sensors, collecting data from an unstructured and dynamic external environment, often in harsh conditions. As such, failures can develop in a camera over time through normal wear and tear (known as incipient failure) or they can fail suddenly (known as abrupt failure) (Li et al., 2020). A failure or fault in a sensor is a divergence from the functional state in at least one given parameter of the system (van Schrick, 1997). A sensor fault can occur due to internal (such as wear and tear) and external (temperature, humidity etc) causes. In RGB cameras, internal causes include dead pixels while external causes include broken lens and condensation. These abrupt failures are hard to detect and would have negative effects on the object detection algorithms - making them hard to accurately detect objects and leading to hallucination. The failures occurring in an automated vehicle (AV) for example, can lead to safety failures resulting in crashes and in some cases, fatalities. Currently, to the best of authors' knowledge, there are no rigorous methods for generating camera based sensor failures (Ceccarelli and Secci, 2022).

In this paper, we will be focusing on the sensor failure occurring due to broken lens, although the process detailed in this paper can be used for any of the camera failures listed in (Ceccarelli and Secci, 2022). Broken or cracked lens in a camera can be caused due to an external object hitting the lens or a result of heat and/or pressure developing suddenly within the camera system. In the

*Equal contribution

†Corresponding author



Figure 1: Object detection error using YOLOv8 on KITTI image due to broken lens - upper - image overlaid with broken lens pattern; lower - clean image

parlance of neural networks, the image with broken lens can be considered as an adversarial sample (see Fig. 1). Researchers have shown that small amounts of corruptions, sometimes difficult to be seen by human eyes, are enough to completely fool the neural networks where a subtle change of inputs can lead to drastic change in outputs, thus known as adversarial samples (Akhtar and Mian, 2018, Carlini and Wagner, 2017, Szegedy et al., 2013). We would like to note that Li et al. (2019) provided a physical camera-based adversarial attack paradigm, which serves as the closest related work in this domain. They presented a modification of the image using a overlay of a translucent, carefully crafted sticker which led to misclassification.

Thus, given all of this previous literature on adversarial sample generation, how is this paper different? The difference stems from the physical process of the broken lens - even though the principal point of the fracture in the lens, the force and angle of incidence may be random, the spread of the fracture and the resulting pattern follows an inherently physical process (being either linear or radial). Generating this kind of adversarial sample can be done using real world procedure, where we use calibrated force on lenses to determine the failure. However, this procedure is expensive and time-consuming. An alternate procedure (and one that is significantly less expensive) would be to simulate fracture on a physics based simulation platform using the material properties of glasses similar to that used in the lens. In this work, we build a fracture simulation based on the randomly generated particles in a triangular mesh and perform stress propagation through the mesh using finite element modeling (FEM) methods.

The fracture simulation produces a triangular mesh at every discrete time state δt , but we also want to generate a rendering of the glass fracture. We utilize the OpenCV library to convert the given mesh to a corresponding broken lens pattern image. We can then learn the combined non-linear mapping of the fracture simulation and the rendering as part of the sensor failure generation. Using a neural network, we can then learn the physical process through which the images of thin glass fractures over discrete time states can be generated given the physical parameters.

We can then generate the adversarial images by overlaying the images with the generated broken lens pattern as a filter for two popular open source datasets - KITTI(Geiger et al., 2013) and MS-COCO (Lin et al., 2014). A common process for testing the generated adversarial images is to find the number of images that are not detected using the adversarial filters. However, in our case, due to the adversarial effect being local, we cannot rely simply on an image based measure. We therefore,

use the adversarial images (similar to the upper figure of Fig. 1) and extract the objects which lie in the region where the fracture exists using the ground truth bounding boxes. We then utilize state-of-the-art object detection neural network algorithm YOLOv8 (Jocher et al., 2023) to find the percentage of objects that fail when the adversarial filters are applied. We have a choice in terms of simulated versus emulated samples and we test the effect of realism of the samples in terms of failure rate. In terms of ablation studies, we aim to understand the distributional differences between real broken glass images collected from the internet and the generated images. We perform dimensionality reduction on the images and test them based on Fréchet Inception distance (FID). We show that while the distributions of simulated and emulated images are not same to the real broken lens distributions, they can create the same adversarial problems for the model.

The specific contributions of the paper are:

- we focus on camera failures as a class of adversarial samples and provide a structured way of generating them,
- we devise a physically sound process for simulation of stress propagation through glass and output an image of the final crack, and
- we present a generative emulator for combined non-linear mapping of the physical process that aims at spanning the subspace of broken glass images.

2 Background

2.1 Physics based adversarial samples

The problem of adversarial sample can be defined as follows: for a model M that classifies an input sample X correctly to its designated class i.e. $M(X) = y_{true}$, adding an error ϵ to the input sample X , results in an altered sample \hat{X} such that $M(\hat{X}) \neq y_{true}$. Thus, the injection of the error ϵ results in an adversarial sample that causes the model to fail.

Although the idea of adversarial manipulation of the model has been identified in the context of machine learning quite some time ago (Dalvi et al., 2004), in the last decade, the focus has squarely been on the adversarial attacks on neural networks (Szegedy et al., 2013, Goodfellow et al., 2014). In these papers, the researchers showed that a small targeted injection of noise, almost imperceptible to the human eye, changed the labels completely (Szegedy et al., 2013) and conversely, images could be generated that looked completely unrecognizable to humans but which had perfect classifications from the DNNs (Nguyen et al., 2015).

While these adversarial samples probe the model for possible failures, they lack any physical realism behind their generation and need access to the model. To address this, some recent research has targeted building physically relevant adversarial samples. One of the first forays into this was made by Kurakin et al. (2018) who targeted the accuracy of the models in the physical world by feeding noisy images from a cell-phone camera that led the model to incorrectly classify a large fraction of the samples. Along the similar vein, Eykholt et al. (2018) demonstrated that real traffic signs can be perturbed with simple physical stickers placed strategically to fool state-of-the-art DL algorithms almost perfectly even with viewpoint changes. Other researchers have placed adversarial images (Kong et al., 2020) or LiDAR surfaces (Tu et al., 2020) to generate samples which fool object detectors. While these prior research use physics in terms of generating the samples, they do not come from modeling a rigorous physical process and we aim to fill this gap in this work.

2.2 Neural emulation of physical simulations

Any physics based process can be succinctly expressed as a function Φ which given a state s_t at time t , control input u_t and external force f_t provides the output state at time $t + \delta t$ as

$$s_{t+\delta t} = \Phi[s_t, u_t, f_t] \tag{1}$$

Emulations of physical simulations have been undertaken in the statistical community since Sacks et al. (1989) published their seminal work on utilizing statistical models to provide efficient predictions of computationally expensive computer models. They modeled the deterministic output from the physical simulation as a stochastic process, which provided a measure of uncertainty of predictions.

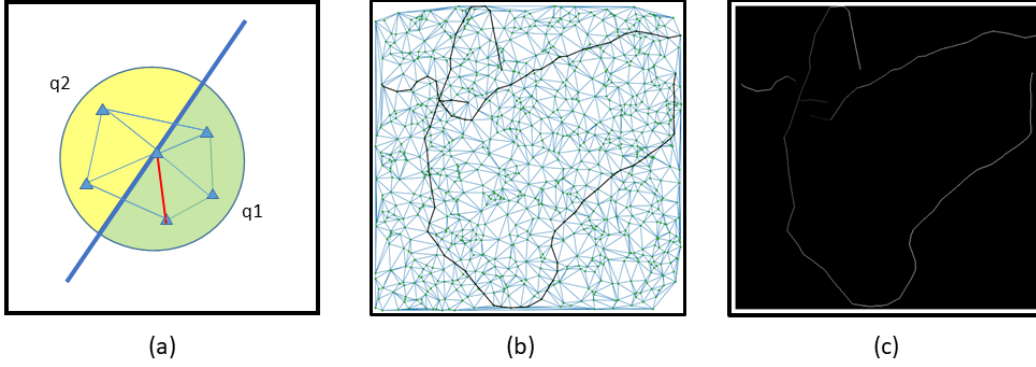


Figure 2: We provide the simulation pipeline for our proposed work - (a) provides a diagram of how the stress propagates in the simulation - for a splitting plane given in blue, the summed positive stress $q1$ and summed negative stress $q2$ are compared and the propagation happens on the side with greater summed stress and chosen node which is the closest to the splitting plane (given in red); (b) shows the triangulated mesh with the fracture; (c) shows the corresponding image

Thus, the statistical models they devise learn an approximation to the dynamic model by observing instances of the state transitions. Since then, a variety of machine learning algorithms have been utilized to perform the emulation process, chief among which is the Gaussian process (Sung and Tuo, 2024). Gaussian process has been shown to have drawbacks in high-dimensional non-linear settings due to the curse of dimensionality (Binois and Wycoff, 2022).

On the other hand, the artificial intelligence community has been building neural network models to emulate high-dimensional, non-linear physical processes which can provide high accuracy but lack in uncertainty quantification (Grzeszczuk et al., 1998). While they started with simple 3-layer feedforward network, in the recent years, with the explosion of deep learning, there has been approaches using deep neural networks to discover constraints between particles or bodies (Battaglia et al., 2016, Han et al., 2022). Particularly, deep graph neural networks have been used successfully to provide physical constraints between particles/bodies (Mrowca et al., 2018, Xu et al., 2019). A related field is the inferring of physics simulations from image frames where the researchers learn the model dynamics from following the object motion in the image frames (Watters et al., 2017). Since, we have access to the physical simulation process, in our proposed work, our goal is to emulate the physical process and then render the image corresponding to the output of the process.

3 Methodology

Generating realistic lens failures require creating large-scale physics based simulations by solving fracture dynamics on a triangulated finite element mesh with glass properties. This triangulated mesh can then be converted into a corresponding image. The image can then be placed as an alpha layer into a captured "clean" image. The entire pipeline for creating a physical simulation and developing an emulation pipeline is described below and in Fig. 2 and 3.

3.1 Broken lens simulation

The subject of how glass breaks and how it propagates is still an open research question and one that has been contentious with multiple physical theories being proposed (Rouxel and Brow, 2012). While the microscopic procedure of glass fracture is being debated on, on a macroscopic level, the fracture dynamics is well understood. Liu et al. (2021) analyzed the process of fracture of glass lens in the precision glass molding application using FEM with a three-dimensional model in a physical simulation software. The physical parameters were input into the software and the crack paths were analyzed using the simulation results. The authors performed a temperature and stress simulation of a high-precision three-dimensional mesh model of the molded glass. Another work which is closely related is the simulation of glass breaking as a thin sheet (Pfaff et al., 2014). Although, the examples

are striking and realistic, the accompanying code for glass did not work as intended. However, these previous works serve as the inspiration.

Glass can be represented using a randomly sampled particles constrained in a mesh or graph. The number and position of the particles within the mesh can be randomly assigned but the mesh is formed using a constrained Delaunay triangulation, which removes ill-shaped triangles and avoids uneven and unrealistic edges as given in Fig. 2(a). Each particle p_i has a position x_i and has nearest neighbors \mathbf{k}_i within a radius r which have existing edges with p_i . Mathematically, the triangulation mesh \mathcal{M} represents a finite set of 2-simplices such that if

$$\forall(K, K') \in \mathcal{M} \times \mathcal{M}, |K| \cap |K'| = |K \cap K'|. \quad (2)$$

The crack patterns in glass occur due to stress from the external force (F) at the initial impact point p_I by assuming a specific deformation law (elasticity, plasticity) of the glass (G) (Kuna, 2013). We then compute the strength parameters in the form of effective stress σ_V at the impact point (V) as the stress state of the impact point. The critical stress values for the strength of glass σ_C is found using tests on simple samples with elementary loading conditions (e.g. tension test). The fracture then occurs when the effective stress is larger than the critical stress divided by the safety factor (S):

$$\sigma_V(G, F) > \frac{\sigma_C}{S}. \quad (3)$$

From the classical theory of strength of materials, we know that the failure in most cases is controlled by the principal stresses σ_I and σ_{II} for 2D elements. The initial crack happens either by the normal-planar crack where the fracture faces are located perpendicular to the direction of the highest principal stress σ_I (Rankine, 1857) or shear-planar crack where the fracture faces coincide with the intersection planes of the maximum shear stress $\tau_{max} = (\sigma_I - \sigma_{II})/2$ (Coulumb, 1776). In the case of glass, we assume that the initial fracture happens perpendicular to the direction of the maximum principal stress.

From the initial impact point p_I , the stress propagation through glass is unstable since the crack grows abruptly without the need to increase external loading. From p_I , stress propagates in the vertex neighborhood \mathbf{k}_i as the stress along the direction $\overrightarrow{p_I p_j}$ where $p_j \in \mathbf{k}_i$ as

$$\sigma_{p_j} = \sigma_V * \frac{\overrightarrow{p_I p_j} \cdot \vec{n}}{|\overrightarrow{p_I p_j}| |\vec{n}|}. \quad (4)$$

With the stress calculated for each edge, the summed positive stress can then be given as:

$$q1 = \int_{\partial\Omega} \sigma_{p_j} \mathbb{I}(\sigma_{p_j} > 0) dA \quad (5)$$

for continuous surface Ω where \mathbb{I} is the indicator function. The summed positive stress for discrete simplices in the corresponding area A of radius R is given as

$$q1 = \sum_{K \in A_R} \sigma_K \mathbb{I}(\sigma_K > 0). \quad (6)$$

Similarly, the summed negative stress $q2$ is calculated. Then for greater magnitude $max(|q1|, |q2|)$, we choose the corresponding edge with the highest concentration of stress in the given segment as the optimal splitting plane since that provides the maximum stress relief. Thus, the stress travel along the mesh edges, dissipating the stress at each node point.

The recursive application of the stress propagation is run until convergence of the stress in all states i.e. $\sigma_p^{(t)} \simeq \sigma_p^{(t-1)} \forall p \in V$. The final output of the simulation is the realization of the graphs as an image which corresponds to broken lens pattern. The pseudo-code for the stress propagation algorithm is given in Algorithm 1.

Even though we provide a relatively low-fidelity simulation, we intended to make it's combined non-linear mappings as realistic as possible. For this we render the crack width and reflection/color based on the stress values. We define the width (W) of a crack using a non-linear transformation for a gradual decay with distance from the impact point and node of maximum stress.

$$W = 1 + \sqrt{\frac{\sigma}{\sigma_{max}}} \times (W_{max} - W_{min}) \quad (7)$$

where W_{max} and W_{min} are chosen discreetly to induce realism.

Algorithm 1 Stress Propagation

```

1:  $pt \leftarrow$  Impact Point
2:  $F \leftarrow$  Impact Force
3:  $PE \leftarrow$  Parent Edge
4:  $v \leftarrow$  Impact Vector
5:  $R \leftarrow$  Nearest neighbor radius
6:
7: procedure PROPAGATESTRESS( $Pt, F, V, PE$ )
8:    $frontiers \leftarrow$   $KDTree - queryRadius(R)$ 
9:    $NN \leftarrow \frac{frontiers-pt}{\|frontiers-pt\|}$ 
10:   $cos(\theta) \leftarrow NN \cdot v$ 
11:   $stress \leftarrow calculateStress(cos(\theta), F)$ 
12:   $frontiers \leftarrow frontiers[argmax(stress)]$ 
13:   $v \leftarrow v[argmax(stress)]$ 
14:   $PE \leftarrow PE[argmax(stress)]$ 
15:  PROPAGATESTRESS( $Pt, F, V, PE$ )
16: end procedure
  
```

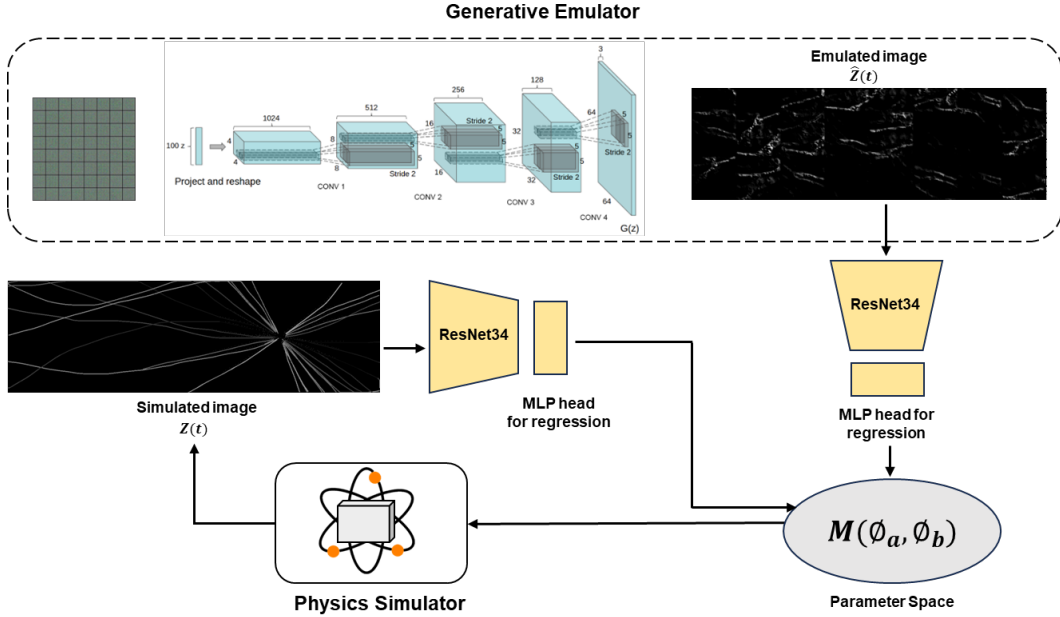


Figure 3: Our neural emulator. We use a ResNet34(He et al., 2016a) architecture to induce physical constraints in our generative branch. The ResNet block is pretrained using the simulated images to learn f_ϕ (Eq. 9). This learnt representation is used to backpropagate the weights of the emulator to generate realistic-physics - guided images

3.2 Neural emulation of physical simulations

Given a simulation, our motive is to emulate the broken glass structure through a physics-informed pipeline. We approach this along the lines of Jiang and Willett (2022) where their objective is to learn an estimation of the parameter space given the given high dimensional simulation output. Since our parameter space is a uniform distribution, we define it as $M(\phi_a, \phi_b)$. We now sample our simulator input from this distribution. Due to its recursive nature, the simulator allows us to create a state-action space by parameterizing the simulation output at any time t using the current state Z_t and the corresponding physical parameters ϕ_t . Then the simulator maps a non-linear function H while adding uniform random noise η to give us the broken glass image (Z). For n samples

($i = 1, 2, 3, \dots, n$), and t timesteps, we then have

$$Z_{i,t} = H(\phi_{i,t-1}) + \eta_i \quad (8)$$

For the emulation, we now learn an inverse function f_ϕ that maps $Z_{i,t}$ to $\phi_{i,t-1}$. We use ResNet34 (He et al., 2016b) as the encoder followed by an MLP head and train it in a supervised fashion to predict ϕ_i . This encoder serves as a physics guide to our generative emulator (see Fig. 3) Given a generator G and a discriminator D , we modify the binary cross-entropy generative loss by adding an additional term for calculating Z 's deviation from M .

$$L_G = -E_{x \sim p(x)}[\log D(G(x))] + \|f_\phi(D(G(x))) - (\phi_a, \phi_b)\| \quad (9)$$

while the discriminator loss is forced to classify any $f_\phi \notin M(\phi_a, \phi_b)$ as a fake image

$$L_D = -E_{Z \sim p(Z)}[\log D(Z)] - E_{x \sim p(x)}[\log(1 - D(G(x)))] \quad (10)$$

where x is some random noise and Z denotes our real/simulated broken glass image. We bind M using physical characteristics like glass toughness, initial force, angle and point of impact.

4 Results

4.1 Benchmarking results

We benchmark three types of broken lens pattern - real, simulated and emulated - on two popular open-source datasets - KITTI(Geiger et al., 2013) and MS-COCO (Lin et al., 2014). The real broken lens pattern images are collected from FreePik website³ and represent the baseline in our case. We collected 65 images in total which we expanded to a set of 10,000 via image augmentation such as random shifts and image flips. Then, we run each image through a random adversarial image and collect the aggregate results. We use a pretrained YOLOv8 model to generate these results. A major shift from most of the previous adversarial examples papers is that our generated adversarial patterns do not affect all pixels in an image universally and therefore, the comparison needs to be done only for the image region where the pattern exists. Therefore, we create a binary mask of each pattern and output the results of the objects which exist in that pattern only.

Table 1: Average precision (in percentage) of different classes in KITTI and MS-COCO under different adversarial images

Dataset	IoU threshold	Class or category	Original	Real	Simulated	Emulated
KITTI	0.25	Pedestrian	32.67	81.39	22.07	87.88
		Truck	12.39	3.85	3.84	33.33
		Car	69.6	61.5	67.2	54.55
	0.5	Pedestrian	25.64	69.72	17.84	83.07
		Truck	12.39	3.59	3.76	33.33
		Car	58.99	50.7	57.73	44.53
	0.75	Pedestrian	6.83	33.88	6.02	37.27
		Truck	11.29	2.67	2.79	33.33
		Car	31.25	23.85	30.15	18.66
MS-COCO	0.25	Person	1.15	0.93	1.13	1.10
		Vehicles	3.45	3.22	5.16	2.43
		Food	35.05	27.98	34.11	9.56
	0.5	Person	0.03	0.02	0.02	0.02
		Vehicles	1.83	1.23	1.54	0.00
		Food	29.11	24.31	26.05	4.69
	0.75	Person	0.03	0.02	0.02	0.00
		Vehicles	1.45	0.92	0.93	0.00
		Food	21.66	16.8	20.95	0.00

Table 1 shows the results of the average precision (AP) under the real, simulated and emulated adversarial images for different classes. For KITTI, the average precision of other classes drop as

³<https://www.freepik.com>

expected with the decrease in AP corresponding to the percentage of image occupied, the truck class recording the highest drop. There is a significant drop for real adversarial images and emulated images, with some drop in the simulated images. A very intriguing and counter-intuitive result is that the pedestrian class has a multiple-fold increase in average precision under real and emulated broken lens patterns.

For MS-COCO, most of the objects occupy smaller image space and its difficult to get meaningful results. Therefore, we have aggregate the AP for the super-categories - person, vehicles and food categories. The emulated images have the highest drop in AP for all the classes with most super-categories not being detected at all, which implies that the emulated image is able to create a much more challenging problem for the model.

	Real	Simulated	Emulated
Real	0.0	181.30	229.81
Simulated	181.30	0.0	269.78
Emulated	229.81	269.78	0.0

4.2 Ablation studies

Given the results above, we would like to understand how close the generated images are to the real broken lens images in the distributional sense. We start by comparing the FID between the given image distributions. FID or 2-Wasserstein distance computes the differences between two image distributions by inputting the distributions through Inception V3 model trained on ImageNet and then uses the two Gaussian distributions generated by a layer to calculate the distance as:

$$d_F(\mathcal{N}(\mu, \Sigma), \mathcal{N}(\mu', \Sigma')) = \|\mu - \mu'\|_2^2 + \text{tr}(\Sigma + \Sigma' - 2(\Sigma\Sigma')^{0.5}) \quad (11)$$

The difference can then be given in the form of a confusion matrix in Fig. 4 where the FID between the same distributions are 0.0 and it increases as the distributions become dissimilar. We see from the confusion matrix, that the simulated images are close in distribution to the real images than the emulated images which makes sense.

Figure 4: FID between real and generated image distributions

5 Discussions

5.1 Implementation of simulation and emulation models

Our simulation model is developed by randomly sampling 10^5 particles from a uniform spatial distribution in the given frame in a CPU. A KD-tree from the SciPy python package (Virtanen et al., 2020) using default parameters is constructed to find the approximate nearest neighbors of each particle. A constrained Delaunay triangulation with an angle threshold of 20° is then run on the particles to create a constrained triangular mesh. We use an impact force of 1000 units with a random impact point and a random impact vector. The stress propagation happens until a threshold of 600 units is reached. The image generation is performed using OpenCV and Python.

We finetune a pretrained ResNet34 feature extractor with an MLP head on 10,000 samples of simulated broken glass images for 30 epochs using the Adam optimizer (Kingma and Ba, 2017) and learning rate of 10^{-3} . We then use this pre-trained model for computing our GAN losses as in Eq. 9 and 10. We train our GAN for 50 epochs, on the same simulated dataset. We use the Adam optimizer for both the generator and discriminator with a learning rate of 2×10^{-4} .

5.2 Limitations

Since the camera failures are governed by physical processes, generation of each kind of camera failure through simulation and then using emulation to learn the state transitions is a computationally expensive process. For some failures such as condensation, the physical process is still not explained to the point where we can build realistic simulations. Therefore, in this paper, we restrict ourselves to broken lens as a particular example of camera failure.

Our physical simulation uses some simplifying assumptions -

- the glass cracks using the maximum principal stress model initially;

- crack propagation happens along the direction of maximum stress relief only;
- multiple paths of stress propagation do not occur;
- no other forces (such as manufacturing defects) are present.

In the generation of adversarial images of broken lens, we have used the generated image without any consideration for visual changes that occur in the fracture due to refraction or glare. Computer graphics software such as Blender or Autodesk Maya can output the visual effects of fracture (without any physical process constraints) which can be incorporated to provide more realistic rendering of broken lens.

The emulated images are not high resolution due to the structure of the GAN network. While this itself is not a hindrance towards creating adversarial images, we would like to have high resolution images in the future.

6 Conclusions

We have introduced a novel class of adversarial failures resulting from the physical process of failures in the camera. In this paper, we provide an approach to generate the broken lens pattern from a physical simulation and subsequently, train a neural network to emulate the physical constraints. We show that the simulated and emulated adversarial images can lead to significant errors in object detection even when the distributions don't span the same space. Our future work will be in performing realistic rendering of the simulated and emulated image. Our aim is to provide a alternative and important means of generating realistic adversarial examples.

References

- Akhtar, N. and Mian, A. (2018). Threat of adversarial attacks on deep learning in computer vision: A survey. *Ieee Access*, 6:14410–14430.
- Battaglia, P., Pascanu, R., Lai, M., Jimenez Rezende, D., et al. (2016). Interaction networks for learning about objects, relations and physics. *Advances in neural information processing systems*, 29.
- Binois, M. and Wycoff, N. (2022). A survey on high-dimensional gaussian process modeling with application to bayesian optimization. *ACM Transactions on Evolutionary Learning and Optimization*, 2(2):1–26.
- Carlini, N. and Wagner, D. (2017). Adversarial examples are not easily detected: Bypassing ten detection methods. In *Proceedings of the 10th ACM workshop on artificial intelligence and security*, pages 3–14.
- Ceccarelli, A. and Secci, F. (2022). Rgb cameras failures and their effects in autonomous driving applications. *IEEE Transactions on Dependable and Secure Computing*.
- Coulumb, C.-A. (1776). Essai sur une application des regles des maximis et minimis a quelques problemes de statique relatifs, a la architecture. *Mem. Acad. Roy. Div. Sav.*, 7:343–387.
- Dalvi, N., Domingos, P., Mausam, Sanghai, S., and Verma, D. (2004). Adversarial classification. In *Proceedings of the tenth ACM SIGKDD international conference on Knowledge discovery and data mining*, pages 99–108.
- Eykholt, K., Evtimov, I., Fernandes, E., Li, B., Rahmati, A., Xiao, C., Prakash, A., Kohno, T., and Song, D. (2018). Robust physical-world attacks on deep learning visual classification. In *Proceedings of the IEEE conference on computer vision and pattern recognition*, pages 1625–1634.
- Geiger, A., Lenz, P., Stiller, C., and Urtasun, R. (2013). Vision meets robotics: The kitti dataset. *International Journal of Robotics Research (IJRR)*.
- Goodfellow, I. J., Shlens, J., and Szegedy, C. (2014). Explaining and harnessing adversarial examples. *arXiv preprint arXiv:1412.6572*.
- Grzeszczuk, R., Terzopoulos, D., and Hinton, G. (1998). Neuroanimator: Fast neural network emulation and control of physics-based model. In *Proceedings of the 25th annual conference on Computer graphics and interactive techniques*, pages 9–20.

- Han, J., Huang, W., Ma, H., Li, J., Tenenbaum, J., and Gan, C. (2022). Learning physical dynamics with subequivariant graph neural networks. *Advances in Neural Information Processing Systems*, 35:26256–26268.
- He, K., Zhang, X., Ren, S., and Sun, J. (2016a). Deep Residual Learning for Image Recognition. In *Proceedings of 2016 IEEE Conference on Computer Vision and Pattern Recognition, CVPR '16*, pages 770–778. IEEE.
- He, K., Zhang, X., Ren, S., and Sun, J. (2016b). Deep residual learning for image recognition. In *Proceedings of the IEEE conference on computer vision and pattern recognition*, pages 770–778.
- Jiang, R. and Willett, R. (2022). Embed and emulate: Learning to estimate parameters of dynamical systems with uncertainty quantification. In Koyejo, S., Mohamed, S., Agarwal, A., Belgrave, D., Cho, K., and Oh, A., editors, *Advances in Neural Information Processing Systems*, volume 35, pages 11918–11933. Curran Associates, Inc.
- Jocher, G., Chaurasia, A., and Qiu, J. (2023). Ultralytics YOLO.
- Kingma, D. P. and Ba, J. (2017). Adam: A method for stochastic optimization.
- Kong, Z., Guo, J., Li, A., and Liu, C. (2020). Physgan: Generating physical-world-resilient adversarial examples for autonomous driving. In *Proceedings of the IEEE/CVF Conference on Computer Vision and Pattern Recognition*, pages 14254–14263.
- Kuna, M. (2013). Finite elements in fracture mechanics. *Solid mechanics and its applications*, 201:153–192.
- Kurakin, A., Goodfellow, I. J., and Bengio, S. (2018). Adversarial examples in the physical world. In *Artificial intelligence safety and security*, pages 99–112. Chapman and Hall/CRC.
- Li, D., Wang, Y., Wang, J., Wang, C., and Duan, Y. (2020). Recent advances in sensor fault diagnosis: A review. *Sensors and Actuators A: Physical*, 309:111990.
- Li, J., Schmidt, F., and Kolter, Z. (2019). Adversarial camera stickers: A physical camera-based attack on deep learning systems. In *International conference on machine learning*, pages 3896–3904. PMLR.
- Lin, T.-Y., Maire, M., Belongie, S., Hays, J., Perona, P., Ramanan, D., Dollár, P., and Zitnick, C. L. (2014). Microsoft coco: Common objects in context. In *Computer Vision—ECCV 2014: 13th European Conference, Zurich, Switzerland, September 6–12, 2014, Proceedings, Part V 13*, pages 740–755. Springer.
- Liu, Y., Xing, Y., Li, C., Yang, C., and Xue, C. (2021). Analysis of lens fracture in precision glass molding with the finite element method. *Applied Optics*, 60(26):8022–8030.
- Mrowca, D., Zhuang, C., Wang, E., Haber, N., Fei-Fei, L. F., Tenenbaum, J., and Yamins, D. L. (2018). Flexible neural representation for physics prediction. *Advances in neural information processing systems*, 31.
- Nguyen, A., Yosinski, J., and Clune, J. (2015). Deep neural networks are easily fooled: High confidence predictions for unrecognizable images. In *Proceedings of the IEEE conference on computer vision and pattern recognition*, pages 427–436.
- Pfaff, T., Narain, R., De Joya, J. M., and O’Brien, J. F. (2014). Adaptive tearing and cracking of thin sheets. *ACM Transactions on Graphics (TOG)*, 33(4):1–9.
- Rankine, W. J. M. (1857). Ii. on the stability of loose earth. *Philosophical transactions of the Royal Society of London*, (147):9–27.
- Rouxel, T. and Brow, R. K. (2012). The flow and fracture of advanced glasses—an overview. *International Journal of Applied Glass Science*, 3(1):1–2.
- Sacks, J., Welch, W. J., Mitchell, T. J., and Wynn, H. P. (1989). Design and analysis of computer experiments. *Statistical science*, 4(4):409–435.
- Sung, C.-L. and Tuo, R. (2024). A review on computer model calibration. *Wiley Interdisciplinary Reviews: Computational Statistics*, 16(1):e1645.
- Szegedy, C., Zaremba, W., Sutskever, I., Bruna, J., Erhan, D., Goodfellow, I., and Fergus, R. (2013). Intriguing properties of neural networks. *arXiv preprint arXiv:1312.6199*.

- Tu, J., Ren, M., Manivasagam, S., Liang, M., Yang, B., Du, R., Cheng, F., and Urtasun, R. (2020). Physically realizable adversarial examples for lidar object detection. In *Proceedings of the IEEE/CVF conference on computer vision and pattern recognition*, pages 13716–13725.
- van Schrick, D. (1997). Remarks on terminology in the field of supervision, fault detection and diagnosis. *IFAC Proceedings Volumes*, 30(18):959–964.
- Virtanen, P., Gommers, R., Oliphant, T. E., Haberland, M., Reddy, T., Cournapeau, D., Burovski, E., Peterson, P., Weckesser, W., Bright, J., van der Walt, S. J., Brett, M., Wilson, J., Millman, K. J., Mayorov, N., Nelson, A. R. J., Jones, E., Kern, R., Larson, E., Carey, C. J., Polat, İ., Feng, Y., Moore, E. W., VanderPlas, J., Laxalde, D., Perktold, J., Cimrman, R., Henriksen, I., Quintero, E. A., Harris, C. R., Archibald, A. M., Ribeiro, A. H., Pedregosa, F., van Mulbregt, P., and SciPy 1.0 Contributors (2020). SciPy 1.0: Fundamental Algorithms for Scientific Computing in Python. *Nature Methods*, 17:261–272.
- Watters, N., Zoran, D., Weber, T., Battaglia, P., Pascanu, R., and Tacchetti, A. (2017). Visual interaction networks: Learning a physics simulator from video. *Advances in neural information processing systems*, 30.
- Xu, Z., Wu, J., Zeng, A., Tenenbaum, J. B., and Song, S. (2019). Densephysnet: Learning dense physical object representations via multi-step dynamic interactions. *arXiv preprint arXiv:1906.03853*.